Practice article

Fast integral terminal sliding mode control with a novel disturbance observer based on iterative learning for speed control of PMSM

Tian Yang [a,b], Yongting Deng [a,*], Hongwen Li [a], Zheng Sun [a,b], Haiyang Cao [a,b], Zongen Wei [a,b]

[a] *Changchun Institute of Optics, Fine Mechanic and Physics, Chinese Academy of Science, Changchun 130033, China*
[b] *The University of Chinese Academy of Sciences, Beijing 100049, China*

ARTICLE INFO

ABSTRACT

This study revolves about the speed control of a permanent magnet synchronous motor (PMSM) with torque ripple and external disturbance. To enhance the performance of the PMSM speed control in response, robustness and torque ripple suppression, a hybrid control technique is presented by combining a novel disturbance observer based on iterative learning strategy (ILC-DOB) and a fast integral terminal sliding mode control (FITSMC) method. Firstly, an iterative learning law is used to enhance the conventional high-gain disturbance observer (DOB) to improve the estimation performance for periodic disturbance. Then, a new fast integral terminal sliding mode surface is proposed to increase the tracking error convergent speed of the traditional integral terminal sliding mode control (ITSMC) when the speed error is distant from the equilibrium point. Finally, the estimated total disturbance is incorporated as a feed-forward compensation to the enhanced FITSMC. According to experimental results, the presented method can ensure better speed-tracking performance and significant disturbance rejection capability of the PMSM drive system.

© 2022 ISA. Published by Elsevier Ltd. All rights reserved.

1. Introduction

Permanent magnet motor has been employed in many transportation systems including electric vehicles and ship propulsion because of its advantages like high energy density, high efficiency and easy maintenance [1]. However, nonlinearity of the motor model, parameters mismatch, and the torque ripple reduce the tracking precision and stability of the servo control system [2–4]. At the same time, the conventional control approach such as proportional–integral (PI) is susceptible to external disturbance and internal parameter uncertainties, which drives the control system away from its desired target.

Therefore, numerous studies devoted to developing appropriate control techniques in the field of PMSM have been carried out [5]. Several nonlinear control methods have been proposed and implemented, e.g., active disturbance rejection control [6], predictive current control [7], internal model control [8], sliding mode control (SMC) [9], and adaptive dynamic programming method [10]. Among them, SMC has been successfully implemented in many types of motors including PMSM due to its benefits like quick response, smaller overshoot and strong disturbance rejection ability. The main drawback of SMC [11], which is mentioned

by many researchers, is the chattering phenomenon. Besides, the conventional SMC method cannot guarantee the robustness of servo system in the approaching phase. Therefore, ITSMC method has been developed [12–14]. Compared with the conventional SMC, ITSMC has the following advantages:

(1) Via setting the initial value of the integral, the system can be in the sliding phase at the beginning, which eliminates the approaching phase and improves the robustness of the system.
(2) Fractional power is applied to guarantee finite-time state convergence during the sliding phase.
(3) Smaller maximum control gain can be selected and the choice of gain only relies on the upper bound of unknown disturbance.

However, all the tracking errors can only be assured to approach to zero in a finite time [15]. The tracking error converges slowly when it is distant from the equilibrium point. Moreover, the upper bound of the lumped disturbance is required to design the control method, which is difficult to be realized in practical application. Then it usually leads to a larger selection of switching gain, which causes more severe chattering.

On the one hand, various methods have been proposed to obtain good dynamic response. An adaptive ITSMC and an adaptive fast ITSMC method [16] are proposed and applied to trajectory

tracking control of underwater vehicles. These two control methods not only guarantee finite-time convergence of the speed tracking to expectation but avoid the demand for the upper bound of lumped disturbance. But, the limitation of these two control strategies is that infinite will appear in the control law, which will lead to potential damage to the inverter and motor. Besides, reaching law approach [17,18] has a direct effect on the approach motion process and is easy to implement. However, the approach time increases when the state nears to the sliding mode surface, and the robustness of the controller decreases. Therefore, this article proposes a new fast integral terminal sliding mode surface that improves the convergent speed when the tracking error is distant from the equilibrium point, and ensures that the tracking error converges to zero within a limited time.

On the other hand, attenuating the chattering phenomenon is another research hotspot to improve SMC quality. In [19], a novel continuous full-order ITSMC strategy is proposed. The chattering phenomenon is attenuated by a full-order sliding-mode design. However, this method requires an acceleration signal, which is difficult to obtain in practice. Disturbance observer-based control is an effective way to attenuate the chattering phenomenon by adding the controller-based feed-forward compensation [20–22]. Its main advantage is improving the disturbance suppression capability without sacrificing the control performance of the compensated system. In [23], an adaptive integral terminal finite-time SMC strategy is proposed and verified on a piezoelectric-driven nanopositioning system. Adaptive laws are developed to estimate the model uncertainty without obtaining the upper boundary of the lumped disturbance. However, this adaptive law can be equivalent to the sliding mode disturbance observer which yields the disturbance estimation with chattering. Then it is brought into the closed-loop system. In [24,25], generalized proportional–integral observer and extended state observer are combined with the SMC, respectively. The performance of these composite controllers depends more on the accuracy of the disturbance estimation. Besides, these traditional disturbance observers are based on that disturbances change slowly over time. However, in actual PMSM working conditions, there are torque ripples which can be regarded as periodic AC disturbances in the speed loop of PMSM systems [26]. Then it will cause periodic fluctuation in the rotational speed, and traditional disturbance observers have limited ability to observe them.

Iterative learning controller (ILC) is a technique that utilizes the control experience of the previous iterative cycles at every current iteration cycle, which has the ability to overcome periodic disturbance. It is widely used in PMSM systems to reject the periodic cogging torque disturbance and is easy to realize in digital systems [27–29]. Therefore, a novel disturbance observer based on iterative learning strategy (ILC-DOB) is proposed in this paper. Iterative learning law is introduced into the conventional disturbance observer to improve estimation performance for the harmonics disturbance. Then, the ILC-DOB is combined with the corresponding FITSMC method to further enhance the robustness and reduce the torque ripple in the PMSM system. The proposed method can not only effectively suppress the phenomenon of torque ripple, but also ensure excellent dynamic response performance and disturbance rejection capability.

The article is organized as follows. Section 2 presents the mathematical model of the PMSM and analyzes the main source of the torque ripples. Section 3 puts forward a novel DOB based on iterative learning principles. In Section 4, two ITSMC algorithms are compared in numerical simulations to demonstrate the advantages of ITSMC. Then, the FITSMC combined with the ILC-DOB is proposed for the PMSM speed controller. In Section 5, comprehensive experiments are carried out to verify the proposed algorithm. Finally, Section 6 concludes this article.

2. Torque ripple analysis and system modeling

Some preliminaries are introduced, such as PMSM models and brief PMSM torque ripple analyses. Then a mathematical model of PMSM considering periodic and aperiodic disturbances is established in this section.

2.1. PMSM model

Neglecting hysteresis losses and eddy currents, the PMSM voltage model in the d-q synchronous rotating reference frame are expressed as

$$\begin{cases} u_d = R_s i_d + L_d \dfrac{di_d}{dt} - p_n \omega_m L_q i_q \\ u_q = R_s i_q + L_q \dfrac{di_q}{dt} + p_n \omega_m (\psi_f + L_d i_d) \end{cases} \quad (1)$$

where, i_d and u_d denote the stator current and voltage of the d-axis, respectively; i_q and u_q denote the stator current and voltage of the q-axis respectively; R_s is stator resistance; L_d, L_q are the d- and q-axis inductances of the stator windings, respectively; p_n is number of pole pairs; ω_m denotes the rotor mechanical angular velocity; ψ_f represents the rotor flux linkage.

The dynamic equation of PMSM is expressed as

$$J \frac{d\omega_m}{dt} = T_e - T_L - B\omega_m \quad (2)$$

where J is rotational inertia; B denotes viscous friction coefficient; T_L is load torque; T_e is electromagnetic torque, which can be expressed as

$$T_e = 1.5 p_n \left[\psi_f i_q + (L_d - L_q) i_d i_q \right] \quad (3)$$

When the surface-mounted PMSM is selected for the drive system, which satisfies $L_d = L_q$, then the electromagnetic torque equation can be expressed as $T_e = 1.5 p_n \psi_f i_q$. In general, the technology of field-oriented control (FOC) is applied to control the PMSM, which has a cascaded double closed-loop structure. In order to obtain d-q axis control voltages, PI controllers are used in the current loops.

2.2. Torque ripple analysis

In the practical application of PMSM, torque smoothness is one of the important indicators to describe performance. However, many non-ideal factors in the motor control systems cause periodic ripples in the output of torque, which in turn lead to speed fluctuations. The torque ripple is mainly produced by magnetic flux harmonics, cogging torque, inverter nonlinearity and current detection error. Considering the above factors, the output electromagnetic torque of PMSM is expressed as

$$\begin{aligned} T_e = \frac{3p_n}{2} (\psi_f + \sum_{i=1}^{\infty} \psi_{6i} \cos(6i\theta_e)) \cdot (\Delta i_{inverter} + \Delta i_{offset} \\ + \Delta i_{scaling} + i_q) + T_{cog} \end{aligned} \quad (4)$$

where θ_e is the electrical angle of the motor; T_{cog} represents the cogging torque of the motor; ψ_f, ψ_{6i} represent the permanent magnet flux and the harmonic amplitude of the 6ith order flux of the motor, respectively; Δi_{offset}, $\Delta i_{scaling}$, $\Delta i_{inverter}$ are current errors caused by the offset and scaling of the current sensors and the nonlinearity of inverters, which can be further expressed as

(5).

$$
\begin{cases}
\Delta i_{inverter} = \dfrac{\omega_e}{\sqrt{R_s^2 + (6\omega_e L_s)^2}}[-A_1\cos(6\theta_e + \theta_5) \\
\qquad\qquad + A_2\cos(6\theta_e + \theta_7) + \dfrac{48V_{dead}}{35\omega_e\pi}\sin(6\theta_e)] \\
\Delta i_{offset} = \dfrac{2}{\sqrt{3}}\sqrt{\Delta i_a^2 + \Delta i_a \Delta i_b + \Delta i_b^2} \cdot \cos(\theta_e + \theta_1) \\
\Delta i_{scaling} = \dfrac{i_s}{\sqrt{3}}(\dfrac{k_a - k_b}{k_a k_b})[\cos(2\theta_e + \dfrac{\pi}{3}) + \dfrac{1}{2}] \\
T_{cog} = \displaystyle\sum_{i=1}^{\infty} T_{cogi}\sin(iN_c\theta_e)
\end{cases}
\tag{5}
$$

In (5), A_1, A_2, θ_5, θ_7 and V_{dead} are the amplitudes of the harmonics, the initial phase angle and the voltage change due to dead-time effects, respectively; Δi_a, Δi_b represent the DC offsets of the phase current i_a, i_b and θ_1 is a constant angle depending on Δi_a and Δi_b; i_s represents the amplitude of the phase current; k_a, k_b represent the scaling factors of the a-phase and b-phase currents, respectively; T_{cogi} represents the amplitude of the ith cogging torque harmonic, and N_c represents the least common multiple between the number of motor cogging and pole pairs.

From (4) and (5), it can be known that the magnetic flux harmonics, the nonlinearity of the inverter and the cogging torque generate the 6th harmonic component in the electromagnetic torque. Besides, current sensor offset produces the 1st harmonic component, and current sensor scaling produces the 2nd harmonic component [30]. Therefore, the electromagnetic torque is mainly composed of DC components and the 1st, 2nd, 6th and 12th harmonic components, which can be simplified as

$$
\begin{aligned}
T_e = T_{e0} + T_{ripple} &= T_{e0} + \sum_k T_{ek}\cos(k\theta_e - \phi_k) \\
&= \frac{3p_n\psi_f}{2}i_q + \sum_k T_{ek}\cos(k\theta_e - \phi_k)
\end{aligned}
\tag{6}
$$

where T_{ripple} represents the torque ripple; k represents the harmonic order; T_{e0} represents the amplitude of the DC component; T_{ek}, ψ_k represent the amplitude and phase angle of the harmonic component, respectively.

Moreover, considering the uncertainty of system parameters and current loop tracking error, the dynamic model of PMSM can be rewritten as

$$
\dot{\omega}_m = \frac{3p_n\psi_{f0}}{2J_0}i_q^* + \varepsilon(t)
\tag{7}
$$

where ψ_{f0} and J_0 represent the nominal values of permanent magnet flux linkage and moment of inertia, separately; i_q^* denotes the reference current of q axis; $\varepsilon(t)$ presents the lumped disturbance, which can be expressed as

$$
\varepsilon(t) = \frac{3p_n\psi_f}{2J}i_q - \frac{3p_n\psi_{f0}}{2J_0}i_q^* - \frac{B}{J}\omega_m - \frac{T_L}{J} - \sum_k \frac{T_{ek}}{J}\cos(k\theta_e - \phi_k)
\tag{8}
$$

From (8), it can be known that the 1st, 2nd, 6th and 12th harmonic components of the electromagnetic torque are included in the lumped disturbance. In Sections 3 and 4, the estimation and compensation of the lumped disturbance will be introduced.

3. Design of iterative learning-based DOB

As a motivation to estimate the above lumped disturbance, a novel disturbance observer ILC-DOB, will be proposed and formulated. Firstly, a high-gain DOB is presented, which can observe

the aperiodic disturbance effectively. Then, an ILC-DOB combined with a high-gain DOB and an iterative learning strategy is presented to suppress the periodic disturbance.

3.1. A high-gain DOB

A first-order system with the external disturbance is used to describe the design procedure, which is represented as follows

$$
\dot{x} = ax + bu + d
\tag{9}
$$

where x denotes the system state, a and b are constant coefficients, u denotes the system control signal, and d denotes the lumped disturbance.

The high-gain DOB can be expressed as

$$
\begin{cases}
\hat{d} = K(x - \hat{x}) \\
\dot{\hat{x}} = a\hat{x} + bu + \hat{d}
\end{cases}
\tag{10}
$$

where, $\hat{x}$, $\hat{d}$ denote the estimated system state and lumped disturbance, separately; K is a constant gain.

Then, we have the following results.

Theorem 1. *If the high-gain DOB is constructed as* (10) *and the parameter K is large enough, the estimation will be converged to the disturbance.*

Proof of Theorem 1. From (10), we have

$$
\dot{\hat{d}} = K(\dot{x} - \dot{\hat{x}}) = K(\dot{x} - a\hat{x} - bu - \hat{d})
\tag{11}
$$

And from (10), we can get $\hat{x} = x - \frac{\hat{d}}{K}$. Together with (11), it implies

$$
\dot{\hat{d}} - a\hat{d} = K(\dot{x} - ax - bu - \hat{d})
\tag{12}
$$

Both sides of (12) are divided by $K(\dot{\hat{d}} - a\hat{d})$, we can obtain

$$
\frac{1}{K} = \frac{\dot{x} - ax}{\dot{\hat{d}} - a\hat{d}} - \frac{bu + \hat{d}}{\dot{\hat{d}} - a\hat{d}}
\tag{13}
$$

When the parameter K tends to infinity, it has

$$
\dot{x} - ax = bu + \hat{d}
\tag{14}
$$

With (9) in mind, we can directly obtain from (14) that $\hat{d} \to d$.

The schematic diagram of the high-gain DOB is shown in Fig. 1. To decrease the influence of measurement noise, a low-pass filter is usually added at the state observation error, where μ is time constant of the low-pass filter. Moreover, in the speed loop of the PMSM system, we have $a = 0$. Thus, the transfer function of the high-gain DOB from the disturbance to the disturbance estimation can be written as

$$
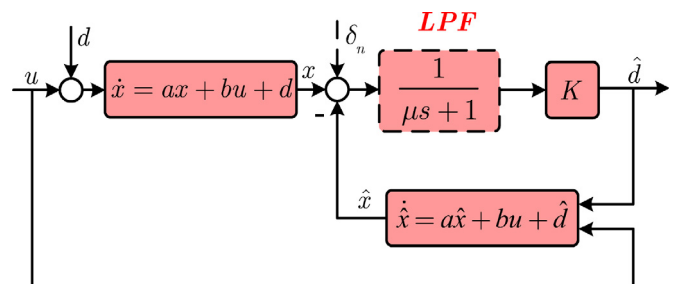G(s) = \frac{\hat{D}(S)}{D(s)} = \frac{K}{s(\mu s + 1) + K}
\tag{15}
$$

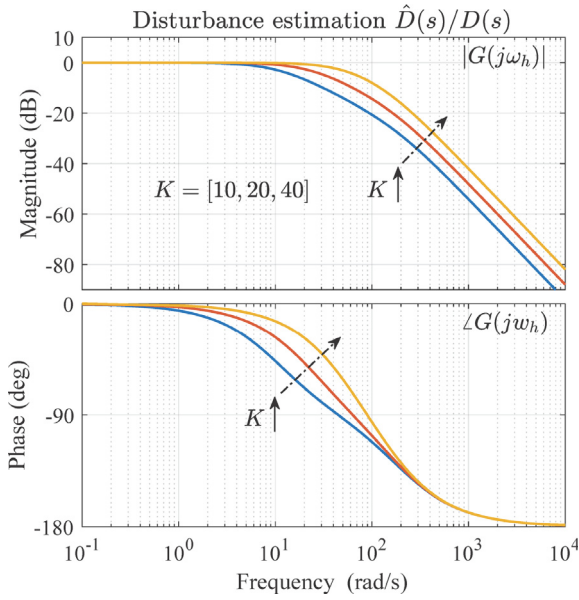**Fig. 1.** Structure diagram of the high-gain DOB.

Fig. 2. Bode plot of disturbance estimation of the high-gain DOB for $K = [10, 20, 40]$.

The bode plot of $G(s)$ is given in Fig. 2. It is clear that a larger K can provide smaller estimation error and phase lag, but the observer's suppression performance for high-frequency noise would be decreased, then the estimation accuracy would reduced in turn. Accordingly, the high-gain DOB can only effectively estimate the DC component of the lumped disturbance.

3.2. Improvement based on iterative learning strategy

To exactly estimate the 1st, 2nd, 6th and 12th periodic harmonic torque, iterative learning control (ILC) is introduced here.

Based on a certain iterative law, ILC applies information from previous experiments to obtain control inputs constantly that produce desired output trajectories. Thus, it is an algorithm that iteratively generates an optimized input signal so that the system output is as close as possible to the ideal. The P-type iterative learning law with a forgetting factor and current cycle feedback is expressed as follows
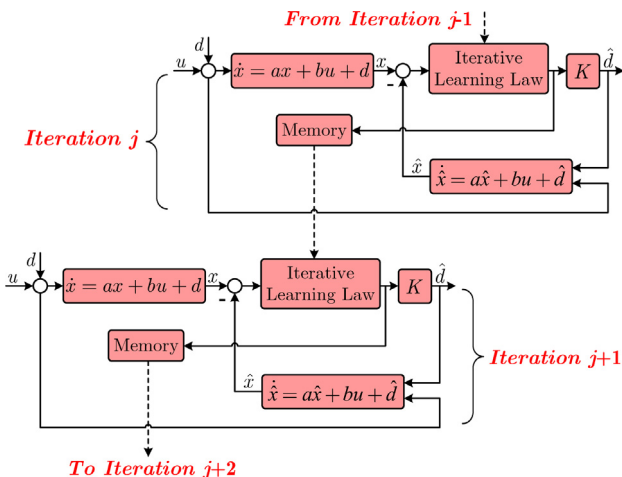
$$u_j(t) = (1 - \xi)u_{j-1}(t) + \gamma e_j(t) \tag{16}$$

where, $u_j(t)$ denotes the control input of the j th iteration, j denotes the iterative index; $e_j(t)$ denotes the tracking error of the j th iteration; γ is the learning coefficient, which affects the learning ability of ILC controller; ξ is the forgetting factor, which can reduce the impact of the non-repetitive disturbance on system convergence. In order to stabilize the ILC algorithm, the value of ξ should be selected in the range of $(0, 1)$.

Firstly, we construct the novel DOB based on the iterative learning strategy, which is depicted in Fig. 3. The ILC-DOB can be written as

$$\begin{cases} \dot{\hat{x}}_j = a\hat{x}_j + bu_j + \hat{d}_j \\ e_j = \gamma(x_j - \hat{x}_j) + (1 - \xi)e_{j-1} \\ \hat{d}_j = Ke_j \end{cases} \tag{17}$$

where $x_j, \hat{x}_j, u_j, d_j$ denote the system state, the estimated system state, the control input and the estimated disturbance for the jth iteration cycle, respectively; e_j, e_{j-1} represent the estimated error of the system state of the jth and j-1th iteration cycles, respectively.

The ILC-DOB's schematic diagram of the transfer function is shown in Fig. 4. To suppress the torque harmonic T_{ripple}, the period of iteration τ, that is, the time delay between e_{j-1} and e_j should be equal to the fundamental period of the torque ripple

$$\tau = \frac{2\pi}{\omega_e} \tag{18}$$

In Fig. 3, the memory unit is responsible for storing the estimate error in the previous iteration and plays a crucial role. For further analysis, it is rewritten as $e^{-\tau s}$ in the complex domain. And referring to (15), we can get

$$G_2(s) = \frac{\hat{D}(S)}{D(s)} = \frac{\gamma K}{s[1 - (1 - \xi)e^{-\tau s}](\mu s + 1) + \gamma K} \tag{19}$$

Compared with (15), the ILC-DOB inserts a delay element in the denominator to extract harmonic disturbances. Considering the disturbance center on the frequency of $6\omega_e$, then $s = j6\omega_e$ and $e^{-\tau s}$ satisfies

$$e^{-\tau s} = e^{-j6\omega_e \tau} = e^{-j12\pi} = 1 \tag{20}$$

According to (20), when $\xi = 0$, (19) equals 1, which indicates that the 6th-order torque harmonic is completely estimated. Similarly, the 12th-order or higher order torque harmonic can be completely observed. When the disturbance is concentrated in a low frequency, $1 - (1 - \xi)e^{-\tau s} < 1$, which indicates that the performance of high-gain DOB in low frequency is also improved effectively.

3.3. Parameters determination for the ILC-DOB

Comparing (15) and (19), it is feasible to select the learning gain $\gamma = 1$ for simplifying analysis and decreasing the parameter
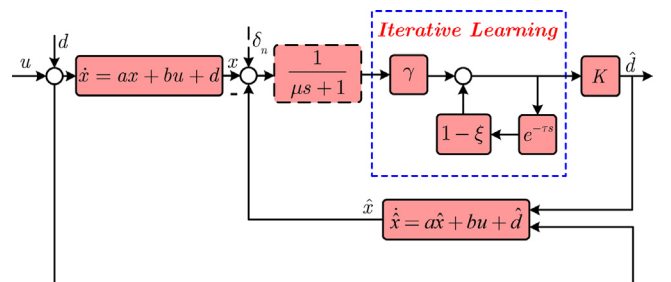

Fig. 3. Structure diagram of the ILC-DOB.

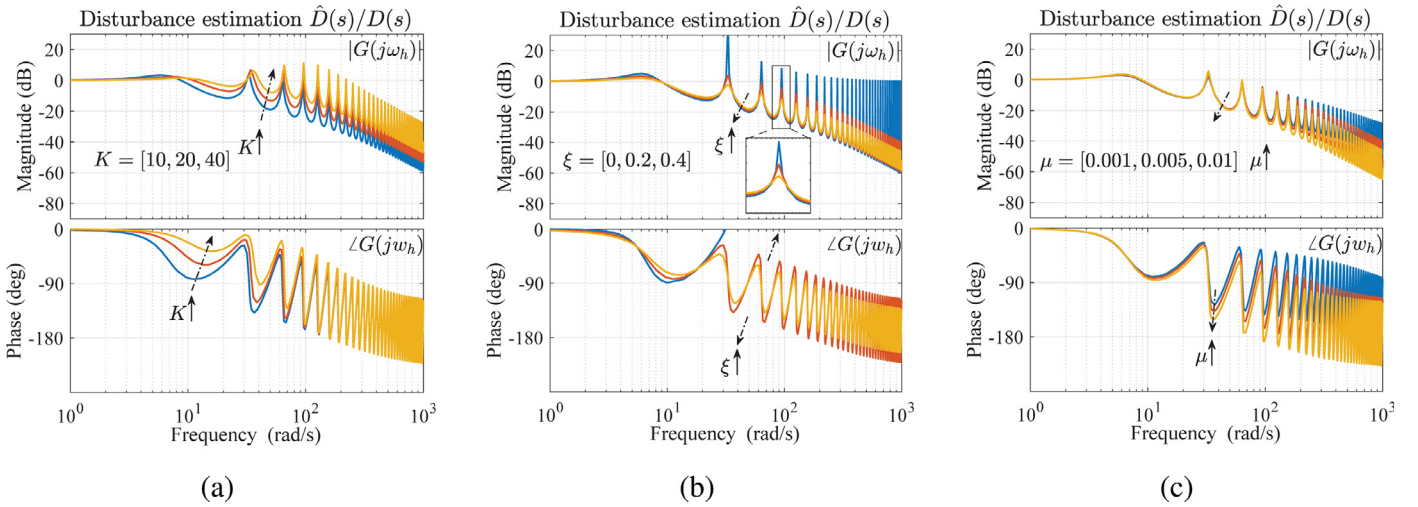**Fig. 4.** Schematic diagram of the transfer function of the ILC-DOB.

Fig. 5. Parameter characteristic of the ILC-DOB with different K, ξ and μ. (a) $\xi = 0.2$, $\mu = 0.005$, $K = [10, 20, 40]$. (b) $K = 20$, $\mu = 0.005$, $\xi = [0, 0.2, 0.4]$. (c) $K = 20$, $\xi = 0.2$, $\mu = [0.001, 0.005, 0.01]$.

tuning workload because γ and K have the same function. Then, parameter characteristic of the ILC-DOB with different K, ξ and μ is given in Fig. 5.

As shown in Fig. 5, the parameter K determines the overall trend of the bode plot, indicating that K affects the estimation performance of the ILC-DOB at low, medium and high frequency. Likewise, ξ affects the peak gain at specific frequencies. And μ influences estimation ability for high-frequency disturbance and noise suppression performance more. Hence, parameters K and ξ are important for the observation performance of the ILC-DOB. The selection of K requires a compromise between the observation error and noise. A basic rule for adjusting K is to increase K from a small initial value till the system performance requirements are satisfied. For the forgetting factor ξ, the conclusion that a smaller ξ will lead to better observation for the periodic disturbance can be drawn from Fig. 5(b). Still, the accumulative effect of the low-frequency non-periodic disturbance is greater, and it has potential to diverge the ILC-DOB. Consequently, the value of ξ cannot be too small and it is typically chosen nearby 0.2. In the speed loop of the PMSM system, μ is typically chosen in the vicinity of 5–10 times than the bandwidth of the speed loop.

4. FITSMC design for PMSM speed loop

The SMC speed controller is adopted to compensate the total disturbance that has been accurately observed. Firstly, the basic ISMC design with sliding mode reaching law (SMRL) method and the proposed FITSMC are given. Then, the first-order system is used to verify the superiority of FITSMC compared with ISMC and ITSMC, respectively.

4.1. ISMC design

The SMC can be designed in two stages: (1) the sliding mode surface design, which forces the system state to reach the equilibrium point of the system; (2) the reaching law design, which guarantees that the trajectory of the system is driven towards the sliding mode surface and remains on it thereafter. The system's robustness is not ensured during the reaching phase of the traditional sliding mode control. To solve this issue, ISMC is introduced to eliminate the reaching phase.

A nonlinear system with the external disturbance is used to describe the ISMC design procedure, which is expressed as

$$\dot{x} = f(x) + g(x)u + d \tag{21}$$

where x is the system state, $f(x)$ and $g(x)$ are the nonlinear functions of x; u denotes the system control signal, and d is the lumped disturbance.

Defining tracking error $e(t) = x_d - x$ (x_d, the desired output), then the ISMC sliding mode surface is designed as

$$s(t) = e(t) + k \int_0^t e(\tau)d\tau \tag{22}$$

where $k > 0$ is a coefficient that needs to be designed.

To speeds up the approaching process and suppress the chattering in the sliding mode surface, a terminal sliding mode reaching law is selected [21]. The terminal sliding mode reaching law is expressed as

$$\dot{s} = -m|s|^\lambda \text{sgn}(s) - ns \tag{23}$$

where m and n are the positive coefficients, and $0 < \lambda < 1$.

4.2. Comparison of two ITSM controller

In (22), when the integration has the initial value $-e(0)/k$, $s(t)$ is initially at zero and hold throughout the system response. On the ISMC manifold $s(t) = 0$, we can derive that

$$e(t) = e(0)\exp(-kt) \tag{24}$$

which cannot ensure that the system state convergences to 0 in a finite time. To overcome this problem, ISMC is combined with the Terminal SMC which can realize finite-time tracking. There are two types of ITSMC named ITSMC1 and ITSMC2, which add a terminal attractor to the proportional term or integral term. When adding the terminal attractor to the proportional term, the ITSMC1 sliding mode surface is as follows [31]:

$$s(t) = \alpha \int_0^t e(\tau)d\tau + e^{p_1/p_2}(t), \alpha > 0 \tag{25}$$

where p_1 and p_2 are positive odd integers satisfying $1 < p_1/p_2 < 2$.

On the other hand, the ITSMC2 can be described as

$$s(t) = e(t) + \beta \int_0^t e^{q_1/q_2}(\tau)d\tau, \beta > 0 \tag{26}$$
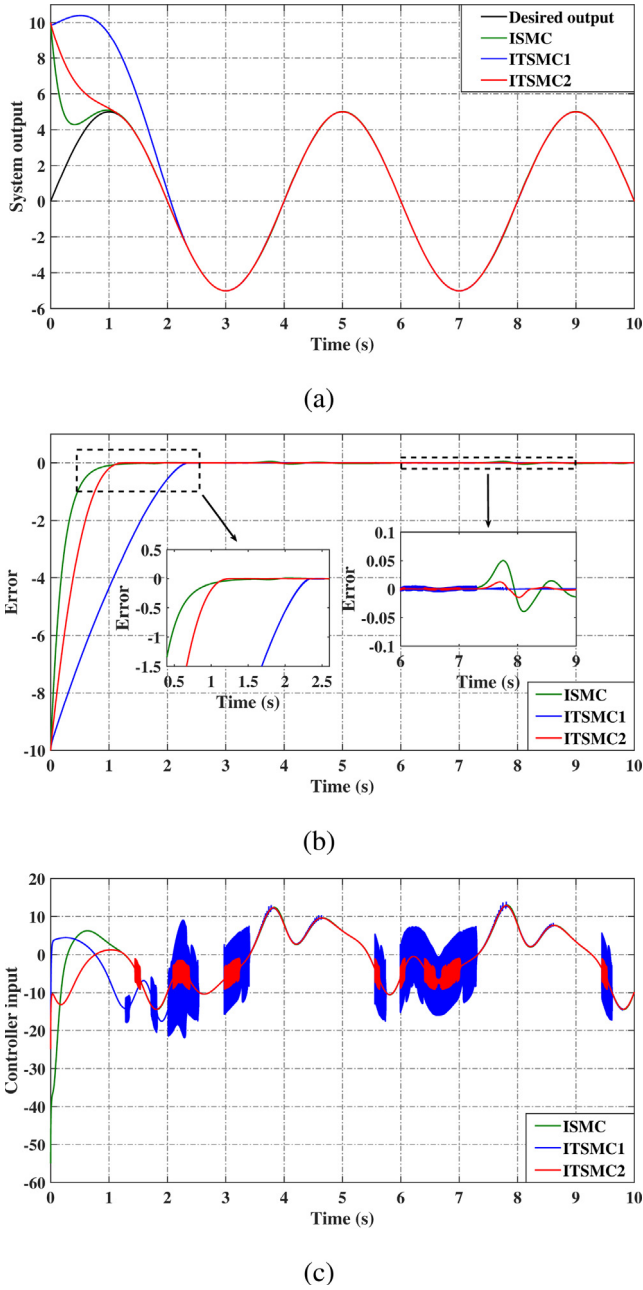
(a)

(b)

(c)

Fig. 6. Simulation waveforms of the ISMC, ITSMC1, and ITSMC2 for the same nonlinear system. (a) System output response. (b) Error response. (c) Control input response.

where q_1 and q_2 are odd integers satisfying $q_2 > q_1 > 0$.

For (25), we defined the integral term $e_I(t) = \int_0^t e(\tau)d\tau$, and assured $e_I(0) = -e^{p_1/p_2}(0)/\alpha$, when $s(t) = 0$, we can derive that

$$T_{f1} = \frac{|e(0)|^{p_1/p_2-1}}{\alpha(1-p_2/p_1)} \tag{27}$$

Similarly, we can derive the convergent time from (26):

$$T_{f2} = \frac{|e(0)|^{1-q_1/q_2}}{\beta(1-q_1/q_2)}, \ (assuring \ e_I(0) = -\frac{e(0)}{\beta}) \tag{28}$$

The performance of the ISMC and two ITSMCs is compared using numerical simulations. System parameters are selected as $f(x) = 5\sin(x)$, $g(x) = 6\mathrm{sgn}(x)$, and $d = 2\sin(\pi t/4)$. Controller parameters are selected $q_1 = 3, q_2 = 5, p_1 = 5, p_2 = 3$ and

$k = \alpha = \beta = 5$. The initial state is set as $x(0) = 10$. The reaching law parameters are set as $m = n = 30, \lambda = 1/3$. Fig. 6 compares the performance of the ISMC, ITSMC1 and ITSMC2. The following conclusions can be obtained from (27), (28) and Fig. 6. These controller have the desirable tracking performance when the control system is influenced by the nonlinear team $f(x), g(x)$ and the disturbance term $d(t)$. When the system error satisfies $|e(t)| \geq 1$, the ISMC reaching speed is more superior than ITSMCs. But when $|e(t)| < 1$, the finite-time convergent advantage of ITSMCs appears. It can be seen that when (27) and (28) have the same denominator, ITSMC1 has faster convergent speed when $|e(t)| < 1$ and is more robust but with unexpected chattering. It is also noticeable that ITSMC1 is singular, because the controller output will be gigantic especially when the error tends to zero.

4.3. FITSMC and controller design

To overcome the shortcomings of the above ISMC and ITSMCs, a FITSMC with fast convergent property is defined as

$$s(t) = e(t) + \int_0^t [\alpha\mathrm{sgn}(e(\tau))+\beta|e(\tau)|^{q_1/q_2}\mathrm{sgn}(e(\tau))]d\tau \tag{29}$$

where $e(t), \beta, q_1, q_2$ are defined the same as in the ITSMC2, $\alpha > 0$ is a constant that requires to be designed.

On the FITSMC manifold $s(t) = 0$, there is

$$\dot{e}(t) = -\alpha\mathrm{sgn}(e(t)) - \beta|e(t)|^{q_1/q_2}\mathrm{sgn}(e(t)) \tag{30}$$

Compared with (26), (29) contains an integral term of $\alpha\mathrm{sgn}(e)$. It ensures that the speed tracking error converges faster when it is distant from the equilibrium point. The beginning value of the integration, $-e(0)$, ensures that $s(t)$ is always remained at zero. Furthermore, by solving (30), the convergent time T_{f3} makes $e(t)$ reach $e(T_{f3}) = 0$ from $e(0)$. Then, T_{f3} is calculated as

$$T_{f3} = \frac{|e(0)|}{2\alpha} + \frac{|e(0)|^{1-q_1/q_2}}{2\beta(1-q_1/q_2)} \tag{31}$$

which indicates that the finite-time convergent advantage of ITSMC is not affected and the FITSMC also offers a faster convergent rate for tracking error than the ITSMC2.

Defining the speed tracking error of the PMSM system $e_\omega = \omega_m^{ref} - \omega_m$, where ω_m^{ref} denotes the mechanical angular velocity reference. Then, the sliding mode surface is designed as

$$s(t) = e_\omega(t) + \int_0^t [\alpha\mathrm{sgn}(e_\omega(\tau))+\beta|e_\omega(\tau)|^{q_1/q_2}\mathrm{sgn}(e_\omega(\tau))]d\tau \tag{32}$$

Taking derivative of (32), and then combining with the reaching law (23) yields

$$\dot{\omega}_m^{ref} - \frac{3p_n\psi_{f0}}{2J_0}i_q^* - \varepsilon(t) + \alpha\mathrm{sgn}(e_\omega) + \beta|e_\omega|^{q_1/q_2}\mathrm{sgn}(e_\omega)$$
$$= -m|s|^\lambda\mathrm{sgn}(s) - ns \tag{33}$$

Thus, the control law can be obtained as

$$i_q^* = \frac{2J_0}{3p_n\psi_{f0}}[m|s|^\lambda\mathrm{sgn}(s) + ns + \dot{\omega}_m^{ref} + \beta|e_\omega|^{q_1/q_2}\mathrm{sgn}(e_\omega)$$
$$+ \alpha\mathrm{sgn}(e_\omega) - \varepsilon(t)] \tag{34}$$

The control law is non-singular, as can be noticed from (34), but the $\alpha\mathrm{sgn}(e_\omega)$ will cause higher chattering than ITSMC2. To minimize chattering brought by the sign function, a sigmoid function is used to replace it, which is given as follows

$$\mathrm{sigmoid}(\mu, e_\omega) = \frac{2}{1 + \exp(-\mu e_\omega)} - 1 \tag{35}$$
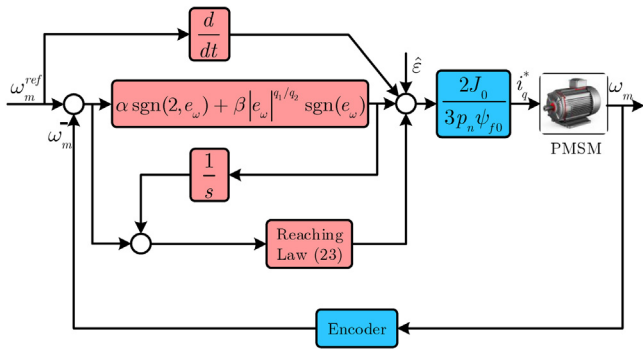
Fig. 7. Block diagram of the FITSMC with ILC-DOB for the speed regulation.

where $\mu > 0$ and $\mu = 2$ is selected to acquire a compromise between the robustness and chattering.

Finally, the control structure of FITSMC with ILC-DOB is shown in Fig. 7. According to Fig. 7, the ILC-DOB firstly estimates the disturbance of the PMSM system, and then feed-forward compensates for the FITSMC controller with the estimation value. And by rewriting (34), the control law is obtained as

$$
\begin{cases}
\dot{\hat{\omega}}_{mj} = \dfrac{3p_n\psi_{f0}}{2J_0}i_{qj}^* + \hat{\varepsilon}_j \\
e_j = \gamma(\omega_{mj} - \hat{\omega}_{mj}) + (1 - \xi)e_{j-1} \\
\hat{\varepsilon}_j = Ke_j \\
i_q^* = \dfrac{2J_0}{3p_n\psi_{f0}}(m|s|^\lambda\mathrm{sgn}(s) + ns + \dot{\omega}_m^{ref} - \hat{\varepsilon}_j + \alpha\mathrm{sigmoid}(2, e_\omega) \\
\qquad + \beta|e_\omega|^{q_1/q_2}\mathrm{sgn}(e_\omega))
\end{cases}
$$
(36)

where ω_{mj}, $\hat{\omega}_{mj}$, i_{qj}^*, $\hat{\varepsilon}_j$ denote the actual and estimated rotor mechanical angular velocity, the reference current of q axis, and the estimated disturbance for the jth iteration cycle, respectively; e_j, e_{j-1} represent the estimated error of the rotor mechanical angular velocity of the jth and j-1th iteration cycles, respectively.

The overall control diagram based on the FITSMC with ILC-DOB is shown in Fig. 8. To analyze the stability of the above FITSMC with ILC-DOB control law, Lyapunov function at jth iteration is constructed as follows

$$V_j = V_j^1 + V_j^2 + V_j^3 \tag{37}$$

where $V_j^1 = |s_j|$, $V_j^2 = \dfrac{1}{2\gamma K}\int_0^t r_j^T r_j d\tau$, $r_j = \varepsilon_j - \hat{\varepsilon}_j$, $V_j^3 = \dfrac{1}{2}(\omega_{mj} - \hat{\omega}_{mj})^2$. s_j is the sliding mode surface of the jth iteration after introducing the ILC-DOB. Substituting (36) into (32), we can get

$$\dot{s}_j = -m|s_j|^\lambda\mathrm{sgn}(s_j) - ns_j - r_j \tag{38}$$

Thus, the change of the first Lyapunov function V_j^1 between two sequent iterations can be derived as:

$$
\begin{aligned}
\Delta V_j^1 &= |s_j| - |s_{j-1}| \\
&= \int_0^t \mathrm{sgn}(s_j)\dot{s}_j d\tau - |s_{j-1}| \\
&= -\int_0^t \mathrm{sgn}(s_j)r_j d\tau + \int_0^t \mathrm{sgn}(s_j)(-m|s_j|^\lambda\mathrm{sgn}(s_j) - ns_j)d\tau \\
&\quad - |s_{j-1}|
\end{aligned}
$$
(39)

The change of the second Lyapunov function V_j^2 between two sequent iterations has the following form:

$$
\begin{aligned}
\Delta V_j^2 &= \frac{1}{2\gamma K}\int_0^t (r_j^T r_j - r_{j-1}^T r_{j-1})d\tau \\
&= \frac{1}{2\gamma K}\int_0^t (\hat{\varepsilon}_{j-1} - \hat{\varepsilon}_j)(2(\varepsilon_j - \hat{\varepsilon}_j) + \hat{\varepsilon}_j - \hat{\varepsilon}_{j-1})d\tau \\
&= -\int_0^t r_j(\omega_{mj} - \hat{\omega}_{mj})d\tau + \frac{\xi}{\gamma}\int r_j e_{j-1}d\tau \\
&\quad - \frac{1}{2\gamma K}\int_0^t (\hat{\varepsilon}_j - \hat{\varepsilon}_{j-1})^2 d\tau
\end{aligned}
$$
(40)

The change of the third Lyapunov function V_j^3 between two sequent iterations can be written as:

$$
\begin{aligned}
\Delta V_j^3 &= \frac{1}{2}(\omega_{mj} - \hat{\omega}_{mj})^2 - \frac{1}{2}(\omega_{mj-1} - \hat{\omega}_{mj-1})^2 \\
&= \int_0^t (\omega_{mj} - \hat{\omega}_{mj})(\dot{\omega}_{mj} - \dot{\hat{\omega}}_{mj})d\tau - \frac{1}{2}(\omega_{mj-1} - \hat{\omega}_{mj-1})^2 \\
&= \int_0^t (\omega_{mj} - \hat{\omega}_{mj})r_j d\tau - \frac{1}{2}(\omega_{mj-1} - \hat{\omega}_{mj-1})^2
\end{aligned}
$$
(41)

The change of the Lyapunov function V_j between jth and j-1th iteration can be obtained by adding above all together.

$$
\begin{aligned}
\Delta V_j &= \Delta V_j^1 + \Delta V_j^2 + \Delta V_j^3 \\
&= -\int_0^t \mathrm{sgn}(s_j)r_j d\tau - n\int_0^t |s_j|\,d\tau - |s_{j-1}| \\
&\quad - \frac{1}{2\gamma K}\int_0^t (\hat{\varepsilon}_j - \hat{\varepsilon}_{j-1})^2 d\tau - \frac{1}{2}(\omega_{mj-1} - \hat{\omega}_{mj-1})^2 \\
&\quad + \int_0^t \mathrm{sgn}(s_j)(-m|s_j|^\lambda\mathrm{sgn}(s_j))d\tau + \frac{\xi}{\gamma}\int_0^t r_j e_{j-1}d\tau
\end{aligned}
$$
(42)

Considering that ξ/γ is relatively small, then the equation mentioned above satisfies

$$\Delta V_j \leq \int_0^t \mathrm{sgn}(s_j)(-m|s_j|^\lambda\mathrm{sgn}(s_j) - r_j)d\tau \tag{43}$$

Let the reaching law coefficient satisfy $m \geq \dfrac{|r_j|}{|s_j|^\lambda}$, then ΔV_j is semi-negative definite and $s \neq 0$, $\Delta V_j < 0$. Therefore, the stability condition of the control law (36) is satisfied. It is guaranteed that the speed tracking error of PMSM system can arrive to 0 from any initial values.
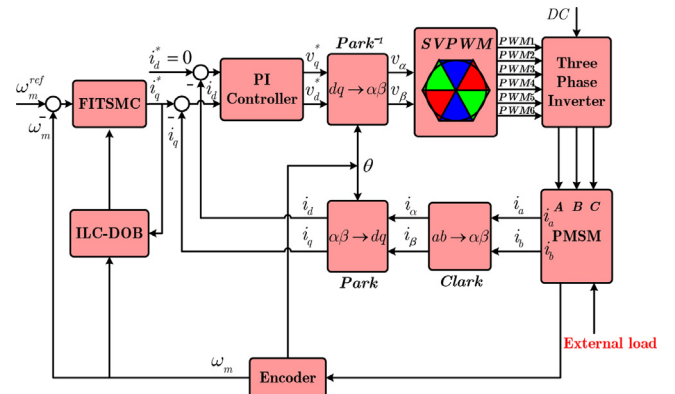

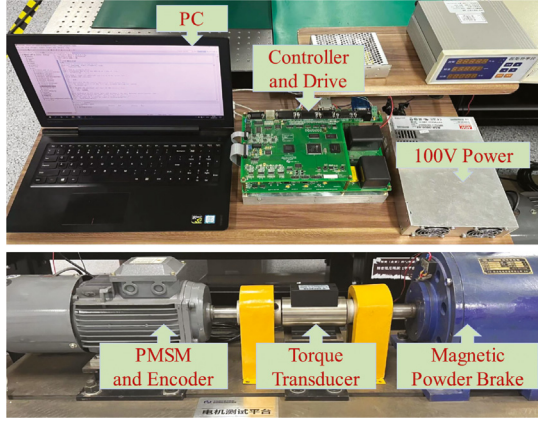
Fig. 8. Structure diagram of the FITSMC with ILC-DOB.

ARTICLE IN PRESS

T. Yang, Y. Deng, H. Li et al.   ISA Transactions xxx (xxxx) xxx

Fig. 9. Photograph of the experimental setup.

Table 1
PMSM parameters.

Parameter	Quantity	Parameter	Quantity
Rated power P_r	5.5 kW	Stator resistance R_s	0.675 Ω
Rated speed S_r	250 rpm	Stator inductance L_s	0.0065 H
Rated torque T_r	10 N m	Flux linkage ψ_f	0.29 V s
Rated currentI_r	7 A	Number of pole pairs p_n	3
Current sample period	100 μs	Inertia J	0.0425 kg m^2
Speed sample period	1 ms	Viscous damping B	0.02 N m s

5. Experimental results analysis

To test the effectiveness of the presented FITSMC with ILC-DOB method, the comparative experiments are performed on a 5.5 kW PMSM hardware platform, as shown in Fig. 9. The proposed FITSMC with ILC-DOB strategy is carried out by a C-program in the 32-bit floating-point DSP TMS320F28335. An 18-bit absolute optical encoder is adopted to precisely acquire the motor speed and position measurement signals. Encoder and A/D data processing, the protection of system fault and generation of inverter switching signals are realized by using the FPGA-EP3C40F324. In the experiment, a magnetic powder brake is applied to produce the external load.

The classical PI, ISMC, ITSMC2 and the presented FITSMC and FITSMC with ILC-DOB methods are studied under different working conditions, which are no-load, sudden load, and sudden unload scenarios. Table 1 presents the main nominal parameters of the PMSM. As a matter of fairness, identical PI current controllers are implemented in the above methods. The parameters of current controllers are: proportional gain $K_{cp} = 2.7$, integral gain $K_{ci} = 340$.

5.1. Step response and disturbance rejection performance

This section discusses the performance of the step response and disturbance rejection between PI, ISMC, ITSMC2 and FITSMC methods. Let above controllers track a step signal ($\omega_m^{ref} = 100$ r/min). Then, the load torque T_L = 1.5 N m is added suddenly at $t = 16$ s and when $t = 25$ s it is removed suddenly to test the disturbance rejection effect. Moreover, the parameters of the PI speed controller are $K_{sp} = 0.07, K_{si} = 0.12$. The parameters of the ISMC, ISMC2 and FITSMC controllers are selected $k = 2, \alpha = 6, \beta = 2, m = 2, n = 10, \lambda = 0.6, q_1 = 3, q_2 = 5$.

Fig. 10 show the speed responses using four different algorithms to a step signal. From Fig. 10(a), it can be obtained that the settling time to 5% tolerance during the startup process is 1.088, 1.274, 2.227, and 1.027 s under PI, ISMC, ITSMC2 and FITSMC methods, separately. Moreover, the settling time to 2% tolerance during the startup process is 1.744, 1.522, 2.477, and 1.354 s under PI, ISMC, ITSMC2 and FITSMC methods, separately. Moreover, it is obvious that the PI controller's speed response contains a 5.185% overshoot and the speed response of the FITSMC controller contains a 2.885% overshoot, while those ISMC and ITSMC2 control methods do not. It is also obvious that the step response of the proposed FITSMC controller has the shortest settling time into the given tolerance in the aforementioned four methods, despite of a mild overshoot. Compared with the ISMC and ITSMC2 methods, the proposed FITSMC controller ensures a faster convergence of the speed tracking error in the entire startup process.

Meanwhile, sudden load and unload experiments are conducted to test the robustness of the conventional PI, ISMC, ITSMC2 and improved FITSMC controllers. Fig. 10(b) and (c) depict the comparing results using the PI, ISMC, ITSMC2, and FITSMC methods under a 1.5 N m load. When the load is added abruptly, the
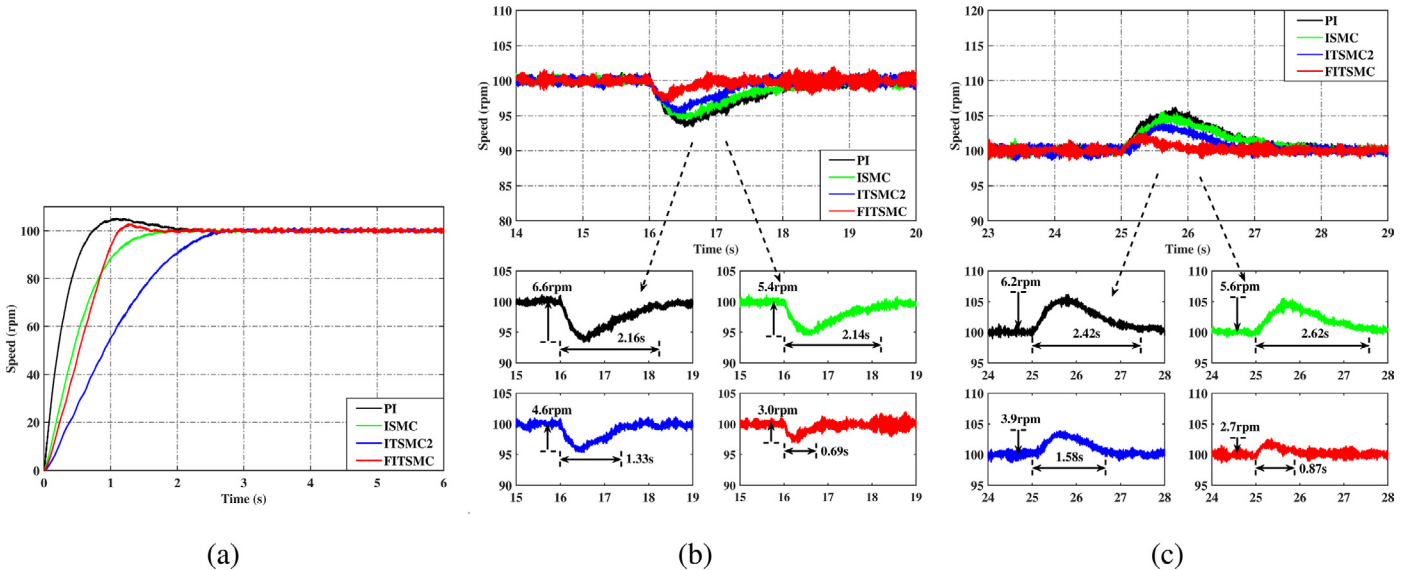

Fig. 10. Speed responses of PI, ISMC, ITSMC2 and FTSMC methods at 100 rpm (a) Step responses under no-load condition. (b) Sudden load responses under 1.5 N m load. (c) Sudden unload responses under 1.5 N m load.

Table 2
Performance comparison during startup and load transient of the PI, ISMC, ITSMC2 and FITSMC methods.

Control method	Startup settling time (s)		Startup overshoot (%)	Speed drop (rpm) and settling time (s) Adding 1.5 N m load		Speed rise (rpm) and settling time (s) removing 1.5 N m load	
	±5%	±2%					
PI	1.088	1.744	5.185	6.6	2.16	6.2	2.42
ISM	1.274	1.522	None	5.4	2.14	5.6	2.62
ITSMC2	2.227	2.477	None	4.6	1.33	3.9	1.58
FITSMC	1.027	1.354	2.885	3.0	0.69	2.7	0.87

speed drop of the PI, ISMC, ITSMC2, and FITSMC methods is 6.6, 5.4, 4.6, and 3.0 rpm, respectively, and the settling time of the PI, ISMC, ITSMC2, and FITSMC methods is 2.16, 2.14, 1.33 and 0.69 s, respectively. When the load is removed suddenly, the speed rise of the PI, ISMC, ITSMC2, and FITSMC methods is 6.2, 5.6, 3.9, and 2.7 rpm, respectively, and the settling time of the PI, ISMC, ITSMC2, and FITSMC methods is 2.42, 2.62, 1.58 and 0.87 s, respectively. The conclusion can be drawn from Fig. 10(b) and (c) that the improved FITSMC has stronger disturbance rejection capability and shorter recovery time than the other controllers. In Table 2, several important performance indices among the PI, ISMC, ITSMC2, and FITSMC methods are listed.

5.2. Torque ripple suppression evaluation

To further investigate the effectiveness of the ILC-DOB on improving disturbance rejection ability and torque ripple minimization, experiments are carried out under sudden load, higher speed (100 r/min) and lower speed (20 r/min) conditions by using the FITSMC and FITSMC with ILC-DOB methods.

Firstly, the observation effect between the traditional high-gain DOB and the ILC-DOB are compared. The experimental parameters of the two types of observers are set as $K = 3$, $\xi = 0.2$, and $\gamma = 1$. The experimental responses of the high-gain DOB and ILC-DOB from no load to 1.5 N m load to no load condition are shown in Fig. 11. As shown in Fig. 11, the ILC-DOB can estimate the lumped disturbance as the high-gain DOB, and the estimated disturbance under the ILC-DOB is much faster than the high-gain DOB when the load torque changes. Moreover, it is clear from the experimental results that the ILC-DOB can observe the lumped disturbance more precisely as expected.

Then, we compare the PMSM regulation system performance at 100 rpm under the FITSMC with ILC-DOB and FITSMC. The experimental results of the FITSMC and FITCMC with ILC-DOB methods are shown in Figs. 12–16. Fig. 12 shows the dynamic
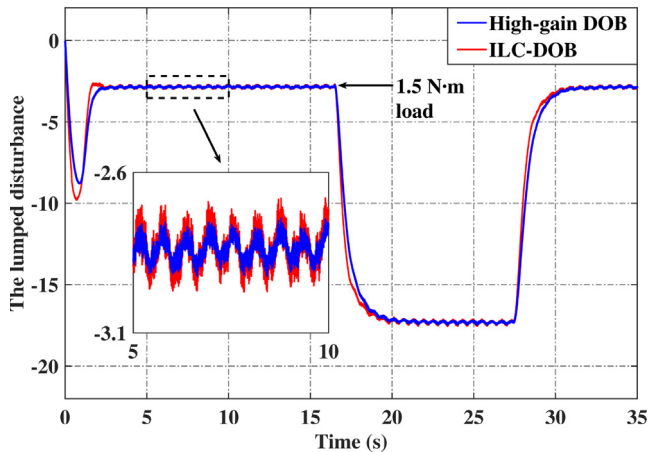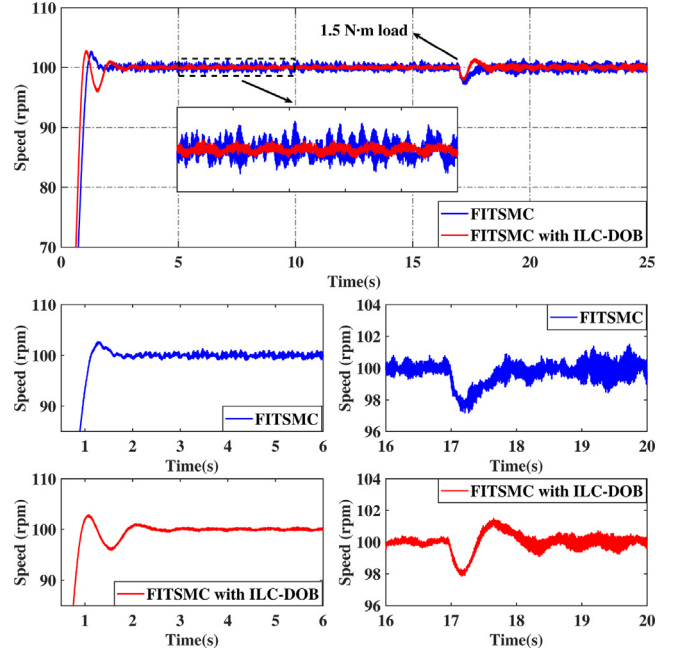

Fig. 12. Sudden load responses of FITSMC, FITSMC with ILC-DOB methods under 1.5 N m load at 100 rpm.

speed responses from no-load startup to sudden load condition. As shown in Fig. 12, when beginning under no-load, the speed response of the FITSMC with ILC-DOB controller contains a 3.01% overshoot. The settling time of the FITSMC with ILC-DOB method to the 5% and 2% tolerance during the starting process are 0.857 and 1.755 s, respectively. It is noticeable that the startup performance between the FITSMC and FITSMC with ILC-DOB methods is approximately close, while the steady-state error of the latter has been reduced from ±1.237 to ±0.513 rpm. Moreover, when the load is added abruptly, the speed response of the FITSMC with ILC-DOB controller drops by 2.1 rpm and after 0.44 s of adjustment, the motor speed returns to the reference. The experimental results validate that the proposed ILC-DOB combined with the corresponding FITSMC has more satisfactory robustness to the disturbance and lower speed ripples.

In order to demonstrate the capability to suppress periodic disturbance of the ILC-DOB, the fast Fourier transformation (FFT) is utilized to analyze the speed fluctuations with the FITSMC and FITSMC with ILC-DOB methods. The speed data in the steady-state period of 5–15 s is employed for FFT analysis and to obtain the 1st, 2nd, 6th and 12th harmonic components. Figs. 13(a) and 14(a) show the steady-state speed response and Figs. 13(b) and 14(b) show the FFT analysis of the related speed. Figs. 13(c) and 14(c) depict the phase current I_a response. As shown in Fig. 13(b), the 1st, 2nd, 6th, and 12th harmonic contents are 0.0715, 0.0280, 0.0029, and 0.0634 rpm, separately. When the ILC-DOB is compensated for the speed loop, the 1st, 2nd, 6th, and 12th harmonic components decrease to 0.0164, 0.0192, 0.0021, and 0.0519 rpm.
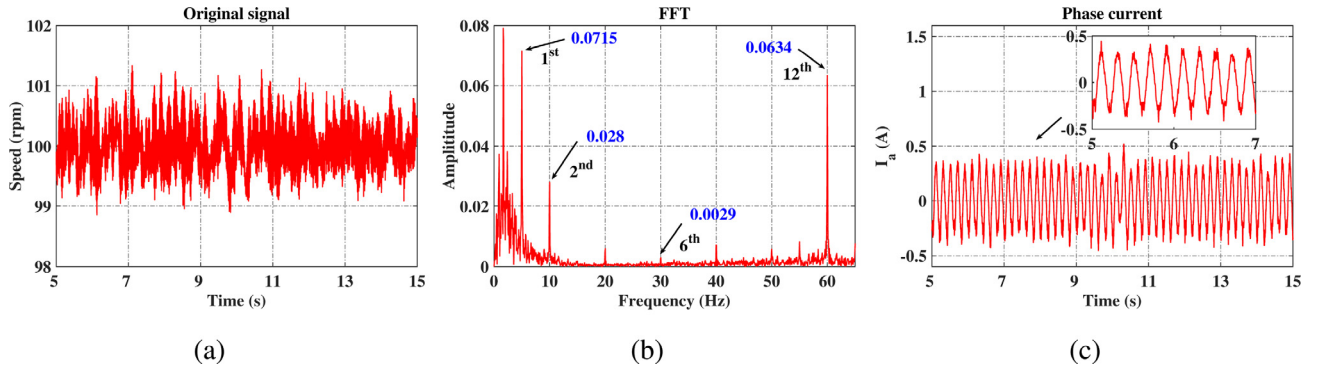

Fig. 11. The estimated lumped disturbance of the high-gain DOB and ILC-DOB under 1.5 N m load.

Fig. 13. Experimental waveforms using the FITSMC method at 100 r/min: (a) speed response; (b) harmonic amplitudes of the speed steady state. (c) I_a response.
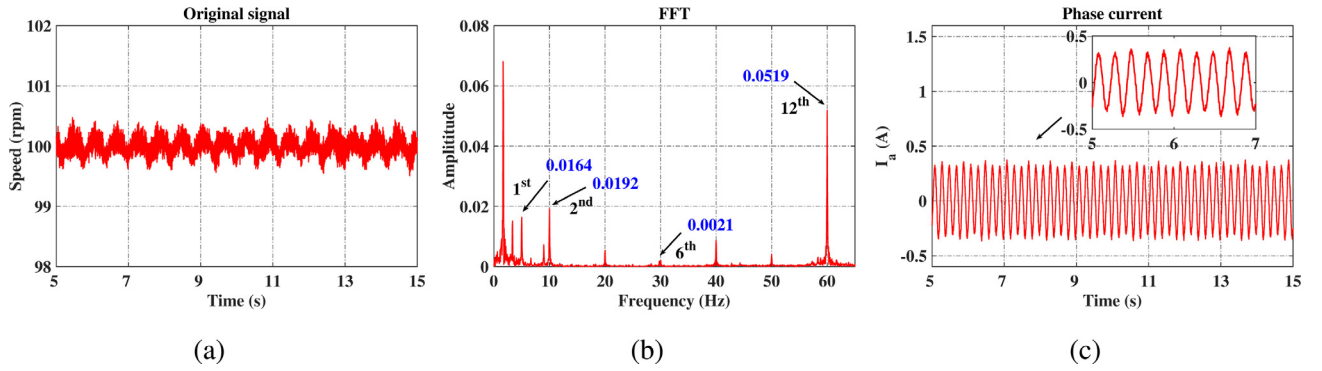

Fig. 14. Experimental waveforms using the FITSMC with ILC-DOB method at 100 r/min: (a) speed response; (b) harmonic amplitudes of the speed steady state. (c) I_a response.
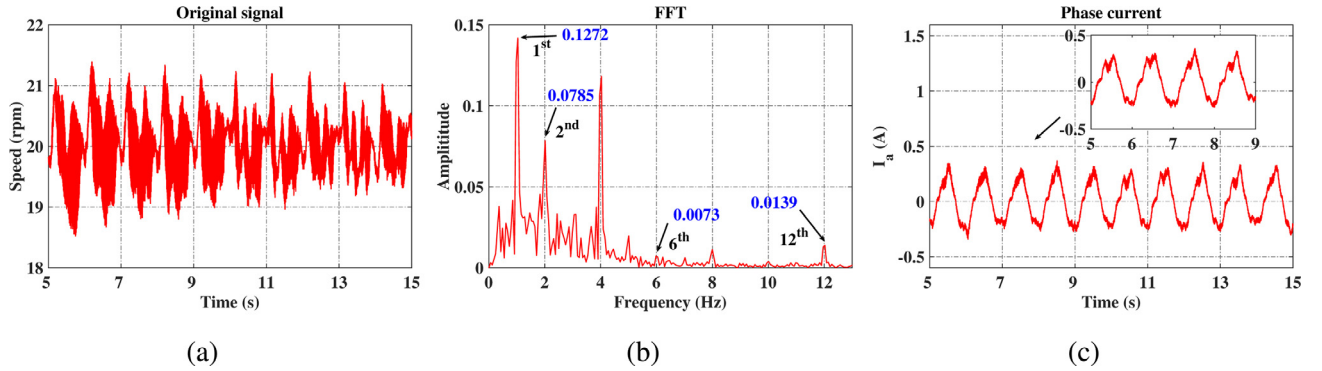

Fig. 15. Experimental waveforms using the FITSMC method at 20 r/min: (a) speed response; (b) harmonic amplitudes of the speed steady state. (c) I_a response.
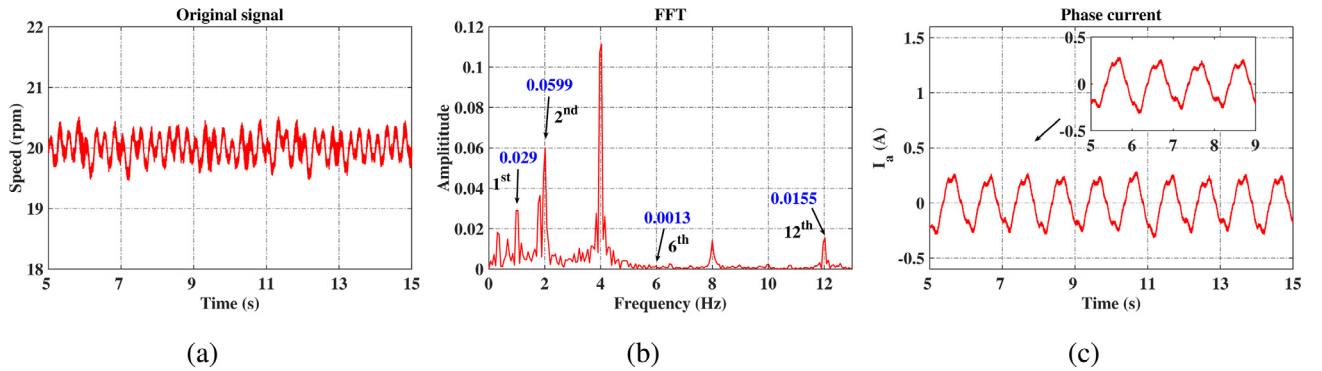

Fig. 16. Experimental waveforms using the FITSMC with ILC-DOB method at 20 r/min: (a) speed response; (b) harmonic amplitudes of the speed steady state. (c) I_a response.
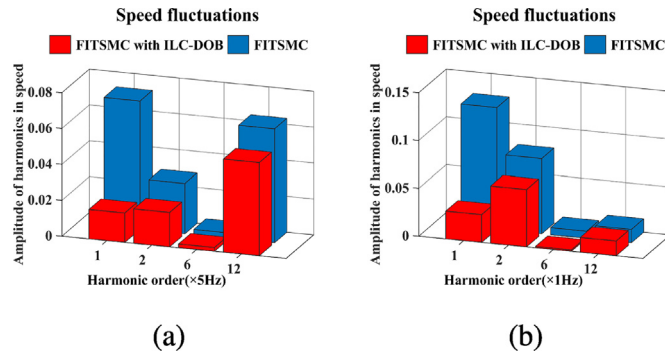
Fig. 17. Harmonic amplitudes comparison between the FITSMC and FITSMC with ILC-DOB methods: (a) at 100 r/min; (b) at 20 r/min.

Simultaneously, the phase current is obviously smoother after the implementation of the ILC-DOB, which indicates that torque ripple is suppressed effectively.

Considering torque ripples are more pronounced when the PMSM operates at a lower speed, experiments are also conducted under lower speed operating condition (20 r/min). Figs. 15(a) and 16(a) show the steady-state speed response at 20 rpm and Figs. 15(b) and 16(b) show the FFT analysis of the related speed. Figs. 15(c) and 16(c) show the phase current I_a response. When the ILC-DOB is compensated for the speed loop, the steady-state error of the FITSMC with ILC-DOB has been reduced from ± 1.433 to ± 0.521 rpm. And as shown in Figs. 15(b) and 16(b), the 1st, 2nd, 6th, and 12th harmonic components decrease from 0.1272, 0.0785, 0.0073 and 0.0139 rpm to 0.0290, 0.0599, 0.0013, and 0.0155 rpm, respectively. Similarly, the phase current is smoother after the implementation of the ILC-DOB.

Additionally, Fig. 17 gives a histogram representation of the harmonic amplitude outcomes of the two different methods. The experimental results indicate that compared with the FITSMC method, the FITSMC with ILC-DOB method ensures torque ripple suppression to a certain extent under both high and low operating speed.

According to the above-mentioned comparative results, it is validated that the proposed FITSMC with ILC-DOB method has the advantages of faster response and better disturbance rejection capability.

6. Conclusion

In this paper, a innovative FITSMC with ILC-DOB strategy is investigated to enhance the disturbance rejection capability and attenuate torque ripple in PMSM system. Compared with the ITSMC controller, the improved FITSMC controller provides a faster error convergent speed when the tracking error is distant from the equilibrium point. In addition, the presented ILC-DOB can effectively estimate the periodic disturbance. After the disturbance estimation of ILC-DOB is feed-forward to the FITSMC controller, the FITSMC with ILC-DOB method can reduce the dynamic speed tracking error and suppress the phenomenon of torque ripple effectively. The superiority of the proposed method is validated by comparing it with traditional methods. This work can be developed further for application to PMSM drive systems with various types of disturbances.

However, when the motor operates under heavy loads, the torque ripples will include more nonintegral order harmonics from the load side, which decreases the estimation performance of the proposed observer. In the future, using adaptive techniques to improve estimation performance for disturbances of nonintegral order harmonics is a promising research direction.

Declaration of competing interest

The authors declare that they have no known competing financial interests or personal relationships that could have appeared to influence the work reported in this paper.

References

[1] Gabbi TS, de Araujo MB, Rocha LR, Scalcon FP, Gründling HA, Vieira RP. Discrete-time sliding mode controller based on backstepping disturbance compensation for robust current control of pmsm drives. ISA Trans 2021.

[2] Liu J, Li H, Deng Y. Torque ripple minimization of pmsm based on robust ilc via adaptive sliding mode control. IEEE Trans Power Electron 2017;33(4):3655–71.

[3] Yin Z, Gong L, Du C, Liu J, Zhong Y. Integrated position and speed loops under sliding-mode control optimized by differential evolution algorithm for pmsm drives. IEEE Trans Power Electron 2019;34(9):8994–9005.

[4] Deng Y, Wang J, Li H, Liu J, Tian D. Adaptive sliding mode current control with sliding mode disturbance observer for pmsm drives. ISA Trans 2019;88:113–26, 2000, 2245–2249.

[5] Zhang W, Cao B, Nan N, Li M, Chen Y. An adaptive PID-type sliding mode learning compensation of torque ripple in pmsm position servo systems towards energy efficiency. ISA Trans 2021;110:258–70.

[6] Qu L, Qiao W, Qu L. Active-disturbance-rejection-based sliding-mode current control for permanent-magnet synchronous motors. IEEE Trans Power Electron 2020;36(1):751–60.

[7] Yu K, Wang Z. Improved deadbeat predictive current control of dual three-phase variable-flux pmsm drives with composite disturbance observer. IEEE Trans Power Electron 2022.

[8] Ping Z, Wang T, Huang Y, Wang H, Lu J-G, Li Y. Internal model control of pmsm position servo system: Theory and experimental results. IEEE Trans Industr Inform 2019;16(4):2202–11.

[9] Komurcugil H, Biricik S, Bayhan S, Zhang Z. Sliding mode control: Overview of its applications in power converters. IEEE Ind Electron Mag 2020;15(1):40–9.

[10] El-Sousy FF, Abuhasel KA. Nonlinear robust optimal control via adaptive dynamic programming of permanent-magnet linear synchronous motor drive for uncertain two-axis motion control system. In: 2018 IEEE industry applications society annual meeting (IAS). IEEE; 2018, p. 1–12.

[11] Yu X, Feng Y, Man Z. Terminal sliding mode control–an overview. IEEE Open J Ind Electr Soc 2020;2:36–52.

[12] Chiu C-S. Derivative and integral terminal sliding mode control for a class of mimo nonlinear systems. Automatica (Oxf) 2012;48(2):316–26.

[13] Qiao L, Zhang W. Adaptive non-singular integral terminal sliding mode tracking control for autonomous underwater vehicles. IET Control Theory Appl 2017;11(8):1293–306.

[14] Zhao Y, Liu X, Yu H, Yu J. Model-free adaptive discrete-time integral terminal sliding mode control for pmsm drive system with disturbance observer. IET Electr Power Appl 2020;14(10):1756–65.

[15] Pal AK, Kamal S, Yu X, Nagar SK, Bandyopadhyay B. Free-will arbitrary time terminal sliding mode control. IEEE Trans. Circuits Syst II Express Briefs 2020.

[16] Qiao L, Zhang W. Double-loop integral terminal sliding mode tracking control for uuvs with adaptive dynamic compensation of uncertainties and disturbances. IEEE J Ocean Eng 2018;44(1):29–53.

[17] Wang Y, Feng Y, Zhang X, Liang J. A new reaching law for antidisturbance sliding-mode control of pmsm speed regulation system. IEEE Trans Power Electron 2020;35(4):4117–26.

[18] Sun X, Cao J, Lei G, Guo Y, Zhu J. A composite sliding mode control for spmsm drives based on a new hybrid reaching law with disturbance compensation. IEEE Trans Transp Electr 2021;7(3):1427–36.

[19] Feng Y, Zhou M, Han Q-L, Han F, Cao Z, Ding S. Integral-type sliding-mode control for a class of mechatronic systems with gain adaptation. IEEE Trans Industr Inform 2019;16(8):5357–68.

[20] Yang J, Chen W-H, Li S, Guo L, Yan Y. Disturbance/uncertainty estimation and attenuation techniques in PMSM drives—a survey. IEEE Trans Ind Electron 2016;64(4):3273–85.

[21] Xu W, Junejo AK, Liu Y, Hussien MG, Zhu J. An efficient antidisturbance sliding-mode speed control method for pmsm drive systems. IEEE Trans Power Electron 2020;36(6):6879–91.

[22] Xu B, Zhang L, Ji W. Improved non-singular fast terminal sliding mode control with disturbance observer for pmsm drives. IEEE Trans Transp Electr 2021;7(4):2753–62.

[23] Xu Q. Adaptive integral terminal third-order finite-time sliding-mode strategy for robust nanopositioning control. IEEE Trans Ind Electron 2020;68(7):6161–70.

[24] Wang J, Wang F, Wang G, Li S, Yu L. Generalized proportional integral observer based robust finite control set predictive current control for induction motor systems with time-varying disturbances. IEEE Trans Industr Inform 2018;14(9):4159–68.

[25] Ma Y, Li D, Li Y, Yang L. A novel discrete compound integral terminal sliding mode control with disturbance compensation for pmsm speed system. IEEE ASME Trans Mechatron 2021.

[26] Feng G, Lai C, Tian J, Kar NC. Multiple reference frame based torque ripple minimization for pmsm drive under both steady-state and transient conditions. IEEE Trans Power Electron 2019;34(7):6685–96.

[27] Wang Y, Gao Y, Zhao C, Li X. Iterative learning based torque ripple suppression of flux-modulation double-stator machine. IEEE Trans Ind Electron 2022;69(7):6645–56.

[28] Mohammed SAQ, Choi HH, Jung J-W. Improved iterative learning direct torque control for torque ripple minimization of surface-mounted permanent magnet synchronous motor drives. IEEE Trans Industr Inform 2021;17(11):7291–303.

[29] Mandra S, Galkowski K, Rogers E, Rauh A, Aschemann H. Performance-enhanced robust iterative learning control with experimental application to pmsm position tracking. IEEE Trans Control Syst Technol 2019;27(4):1813–9.

[30] Huang M, Deng Y, Li H, Wang J. Torque ripple suppression of pmsm using fractional-order vector resonant and robust internal model control. IEEE Trans Transp Electr 2021;7(3):1437–53.

[31] Qiao L, Zhang W. Trajectory tracking control of AUVs via adaptive fast nonsingular integral terminal sliding mode control. IEEE Trans Industr Inform 2019;16(2):1248–58.